



1 **Effects of Coupling a Stochastic Convective Parameterization**  
2 **with Zhang-McFarlane Scheme on Precipitation Simulation in**  
3 **the DOE E3SMv1 Atmosphere Model**

4  
5 Yong Wang<sup>1</sup>, Guang J. Zhang<sup>2\*</sup>, Shaocheng Xie<sup>3</sup>, Wuyin Lin<sup>4</sup>, George C. Craig<sup>5</sup>, Qi Tang<sup>3</sup>, Hsi-  
6 Yen Ma<sup>3</sup>

7  
8 <sup>1</sup>Ministry of Education Key Laboratory for Earth System Modeling & Department of Earth  
9 System Science, Tsinghua University, Beijing, 100084 China

10 <sup>2</sup>Scripps Institution of Oceanography, La Jolla, CA, USA

11 <sup>3</sup>Lawrence Livermore National Laboratory, CA, USA

12 <sup>4</sup>Brookhaven National Laboratory, Upton, NY, USA

13 <sup>5</sup>Meteorologisches Institut, Ludwig-Maximilians-Universität, Munich, Germany

14

15

16

17

18

19

20 Submitted to *GMD*

21 July 28, 2020

22 *Corresponding author:* Guang J. Zhang (gzhang@ucsd.edu)

23



24 **Abstract.** A stochastic deep convection parameterization is implemented into the U.S. Department  
25 of Energy (DOE) Energy Exascale Earth System Model (E3SM) Atmosphere Model version 1  
26 (EAMv1). This study evaluates its performance on the precipitation simulation. Compared to the  
27 default model, the probability distribution function (PDF) of rainfall intensity in the new  
28 simulation is greatly improved. Especially, the well-known problem of “too much light rain and  
29 too little heavy rain” is alleviated over the tropics. As a result, the contribution from different rain  
30 rates to the total precipitation amount is shifted toward heavier rain. The less frequent occurrence  
31 of convection contributes to the suppressed light rain, while both more intense large-scale and  
32 convective precipitation contribute to the enhanced heavy total rain. The synoptic and  
33 intraseasonal variabilities of precipitation are enhanced as well to be closer to observations. A  
34 sensitivity of the rainfall intensity PDF to the model vertical resolution is identified and explained  
35 in terms of the relationships between convective precipitation and convective available potential  
36 energy (CAPE) and between large-scale precipitation and resolved-scale upward moisture flux.  
37 The annual mean precipitation is largely unchanged with the use of the stochastic scheme except  
38 over the tropical western Pacific, where a moderate increase in precipitation represents a slight  
39 improvement. The responses of precipitation and its extremes to climate warming are similar with  
40 or without the stochastic deep convection scheme.  
41



## 42 **1. Introduction**

43 Precipitation plays a vital role in the Earth's climate: the latent heat released during  
44 precipitation formation is a major energy source that drives the atmospheric circulation, and the  
45 precipitation is an important part of the Earth's hydrological cycle. The accurate simulation of  
46 precipitation in global climate models (GCMs) is of great scientific and societal interest. However,  
47 GCMs used for current climate simulation and future projections suffer from many biases in the  
48 global distribution, frequency and intensity of simulated precipitation (Dai, 2006), which have  
49 negatively impacted the model's fidelity. Rainfall in nature is tightly associated with many  
50 complex dynamic and physical processes in the atmosphere, including large-scale circulation,  
51 convection, cloud microphysics, and planetary boundary layer (PBL) processes. The deficiencies  
52 in representing these processes in GCMs are prime culprits for errors in simulated rainfall (Watson  
53 et al., 2017).

54 Among the physical processes in GCMs, the parameterization of convection is responsible  
55 for some well-known biases: the double Intertropical Convergence Zone (Zhang and Wang 2006;  
56 Zhang et al., 2019), too weak synoptic and intraseasonal variabilities in the tropics (Zhang and Mu,  
57 2005a; Watson et al., 2017), the wrong diurnal cycle of rainfall (Xie et al., 2019), "too much light  
58 rain and too little heavy rain" (Dai, 2006; Zhang and Mu, 2005b; O'Gorman and Schneider, 2009),  
59 to name a few. The conventional deterministic convective parameterization in GCMs represents  
60 the ensemble effects of subgrid-scale convective clouds in a model grid box on resolved scale  
61 variables. However, in reality, a given grid-scale state may lead to different realizations of subgrid-  
62 scale convection (Davies et al., 2013; Peters et al., 2013) rather than to a single "ensemble-mean"  
63 response. For instance, two model grid boxes, both in a similar convective-equilibrium state, can  
64 have different numbers and/or sizes of convective clouds due to stochasticity (Cohen and Craig,  
65 2006). This stochasticity will appear more frequently as the model grid-box size becomes smaller  
66 (Jones and Randall, 2011). Not including stochasticity in convective schemes has been suggested  
67 to be at least partly responsible for the weak intraseasonal variability and "too much light rain and  
68 too little heavy rain" in GCMs (Lin and Neelin 2000, Wang et al., 2016; Watson et al., 2017; Peters  
69 et al., 2017).

70 As suggested in Palmer (2001, 2012), more realistic statistics of the impacts of subgrid  
71 convective clouds should be derived by simulating them as random samples from probability  
72 distributions conditioned on the grid-scale state, so that the influences of different individual  
73 realizations are introduced in the convection parameterization. In this regard, much effort in the



74 past two decades has been made to develop stochastic convection schemes (e.g., Lin and Neelin,  
75 2000, 2002; Plant and Craig, 2008; Khouider et al., 2010; Sakradzija et al., 2015). Among these  
76 schemes, Plant and Craig (2008) (PC08 hereafter) developed a stochastic deep convection  
77 parameterization under a framework based on statistical mechanics (Cohen and Craig, 2006; Craig  
78 and Cohen, 2006) for noninteracting convective clouds in statistical equilibrium using cloud-  
79 resolving model (CRM) simulations. This scheme was applied to numerical weather prediction  
80 (NWP) models and to a GCM in an aquaplanet setting, resulting in some substantial improvements  
81 in precipitation simulation (Groenemeijer and Craig, 2012; Keane et al., 2014, 2016).

82 Wang et al. (2016) incorporated the PC08 stochastic deep convection scheme into the Zhang-  
83 McFarlane (ZM) deterministic deep convection scheme (Zhang and McFarlane, 1995) in the  
84 National Center for Atmospheric Research (NCAR) Community Atmosphere Model version 5  
85 (CAM5). They found that the introduction of the stochastic scheme improved the simulation of  
86 precipitation intensity and intraseasonal variability over the tropics in CAM5 (Wang and Zhang  
87 2016; Wang et al., 2017).

88 In this study, we implement the PC08 stochastic deep convection parameterization scheme  
89 into the DOE Energy Exascale Earth System Model (E3SM) (Golaz et al. 2019) Atmosphere  
90 Model version 1 (EAMv1) (Rasch et al. 2019; Xie et al. 2018) and examine its effect on  
91 precipitation simulation. The EAMv1 is branched out from CAM5 and thus it inherits many model  
92 deficiencies from CAM5 as well. Many modifications in physics parameterizations have been  
93 made compared to CAM5 (Rasch et al. 2019; Xie et al. 2018). However, some model biases such  
94 as weak precipitation intensity persist (Xie et al. 2019). Thus, besides the precipitation metrics  
95 explored in our previous studies (Wang et al. 2016, 2017; Wang and Zhang 2016), this study will  
96 evaluate precipitation simulation with more systematical metrics. In addition, the responses of  
97 precipitation and its extremes to climate warming with the stochastic deep convection scheme will  
98 be investigated.

99 The organization of the paper is as follows. Section 2 presents parameterization, model,  
100 experimental design, and evaluation data. Section 3 describes results, including variability,  
101 frequency, intensity, amounts, duration, mean state, and responses of precipitation and its extremes  
102 to climate warming. The sensitivity of the rainfall intensity pdf to vertical resolution and  
103 underlying mechanisms are also presented in this section. Summary is given in section 4.

104

## 105 **2. Parameterization, model, experimental design and evaluation data**



## 106 2.1. Stochastic deep convection parameterization

107 The stochastic convective parameterization scheme of PC08 is modified for climate models  
108 when incorporating into the ZM deterministic deep convection scheme. In the PC08 scheme, the  
109 probability of launching one convective cloud is given by:

$$110 \quad p_{d\bar{n}(m)}(n = 1) = \frac{1}{\langle m \rangle} e^{-m/\langle m \rangle} \langle N \rangle dm \quad (1)$$

111 where  $d\bar{n}(m)$  denotes the average number of clouds with mass flux between  $m$  and  $m+dm$ ,  $\langle m \rangle$   
112 is the ensemble mean mass flux of a cloud, and  $\langle N \rangle$  is the ensemble mean number of convective  
113 clouds in a given GCM grid box ( $\langle N \rangle = \langle M \rangle / \langle m \rangle$ , with  $\langle M \rangle$  the ensemble mean total cloud mass  
114 flux given by the closure in the ZM deterministic parameterization). For each mass flux bin,  
115 whether to launch a cloud is determined by comparing the probability from Eq. (1) with a random  
116 number uniformly generated between zero and one which, unlike the update frequency of once a  
117 day in Wang et al. (2016), is updated every 3 days in consideration of computational resources due  
118 to finer vertical and horizontal resolutions in the EAMv1 (see section 2.2). For the same reason,  
119 the spatial averaging of input quantities (i.e., vertical profiles of temperature and moisture) to the  
120 stochastic scheme over neighboring grid points used in the original design of PC08 is not  
121 performed because it leads to an excessive communication load. One can argue that at a horizontal  
122 model resolution of about 110 km in EAMv1, convective quasi-equilibrium approximately holds  
123 over some timescale although at individual model timestep it does not. Thus, although spatial  
124 averaging is not applied, the temporal trailing averaging over 3 h at each time step is retained in  
125 the scheme. Other modifications to the PC08 scheme for incorporation into the ZM scheme in  
126 climate models (Wang et al. 2016) are retained. These include:

127 1) The temporally averaged quantities are used to calculate the ensemble mean cloud mass  
128 flux ( $\langle M \rangle$ ), which is determined by the ZM scheme. The unsmoothed grid point quantities are still  
129 used in the trigger function and the cloud model.

130 2) The root mean squared cloud radius information originally used in PC08 is not needed in  
131 our implementation because the ZM scheme does not use cloud radius.

132 3) The ensemble mean mass flux of a cloud  $\langle m \rangle$  is set to  $1 \times 10^7$  kg s<sup>-1</sup> following  
133 Groenemeijer and Craig (2012).

134 4) The cloud life cycle effect with a factor  $dt/T$  ( $dt$  is the model time step and  $T$  is the constant  
135 lifetime parameter) in PC08 is not taken into account because the ZM deterministic  
136 parameterization does not consider the life cycle of convection.



137           5) The mass fluxes from all clouds in a GCM grid box generated from eq. (1) are rescaled by  
138 a factor  $\langle N \rangle$  to account for the fact that there can be many clouds in a GCM grid box.

139

## 140 **2.2. EAMv1 model**

141           The standard configuration of the DOE EAMv1 uses a spectral element dynamical core at  
142 110-km horizontal resolution on a cubed sphere geometry and a vertical resolution of 72 layers  
143 from the surface to 60 km (10 Pa) (Rasch et al. 2019, Xie et al. 2018). The treatment of PBL  
144 turbulence, shallow convection, and cloud macrophysics are unified with a simplified third-order  
145 turbulence closure parameterization CLUBB (Cloud Layers Unified by Binormals, Golaz et al.,  
146 2002; Larson and Golaz, 2005). The deep convection is represented by the ZM scheme. The  
147 Morrison and Gettelman (2008) (MG) microphysics scheme is updated to MG2 (Gettelman et al.,  
148 2015) with the prediction of rain and changes to ice nucleation and ice microphysics (Wang et al.,  
149 2014). A four-mode version of the modal aerosol module (MAM4) (Liu et al., 2016) is used with  
150 improvements to aerosol resuspension, aerosol nucleation, scavenging, convective transport and  
151 sea spray emissions for including the contribution of marine ecosystems to organic matter (Rasch  
152 et al., 2019). A linearized ozone chemistry module (Hsu and Prather, 2009; McLinden et al., 2000)  
153 is used to represent stratospheric ozone and its radiative impacts in the stratosphere. Other  
154 modifications for model tuning are provided in detail in Xie et al. (2018).

155

## 156 **2.3. Experimental design**

157           Six Atmospheric Model Intercomparison Project (AMIP) type simulations are conducted.  
158 Four 6-year simulations are forced by prescribed, seasonally varying climatological present-day  
159 sea surface temperatures (SSTs) and sea ice extent, recycled yearly (Stone et al., 2018): two with  
160 the default deterministic ZM scheme but having 72 and 30 vertical levels respectively (referred to  
161 as EAMv1 and EAMv1-30L) and the other two with the stochastic deep convection scheme  
162 (referred to as STOCH and STOCH-30L). The simulations with 30 vertical levels are conducted  
163 to facilitate the comparison with Wang et al. (2016), in which the vertical resolution of CAM5 is  
164 30 levels (see section 3.3). To explore the responses of precipitation and its extremes to climate  
165 warming, similar to EAMv1 and STOCH runs, two 3-year simulations in a warmer climate are  
166 conducted, in which a composite SST warming pattern derived from the Coupled Model  
167 Intercomparison Project Phase 3 (CMIP3) coupled models (referred to as EAMv1-4K and  
168 STOCH-4K respectively) is imposed for the boundary condition of the atmosphere. Following



169 Webb et al. (2017), it is a normalized multi-model mean of the sea surface temperature response  
170 pattern from 13 CMIP3 atmosphere-ocean general circulation models, representing the change of  
171 SST between years 0-20 and 140-160, the time of CO<sub>2</sub> quadrupling in the 1% runs. Before  
172 calculating the multi-model ensemble mean, the SST response of each model was divided by its  
173 global mean and multiplied by 4K. This guarantees that the pattern information from all models is  
174 weighted equally and that the global mean SST forcing is +4K warming. The first year in all  
175 simulations is discarded as a spin-up. Information for all experiments is summarized in Table 1.

176

#### 177 **2.4. Evaluation data**

178 For model evaluation, the following datasets are used: The Clouds and the Earth's Radiant  
179 Energy System Energy Balanced and Filled (CERES-EBAF) (Loeb et al., 2009) for evaluation of  
180 shortwave and longwave cloud radiative forcing; the Interim European Centre for Medium-Range  
181 Weather Forecasts Re-Analysis (ERA-Interim) (Simmons et al., 2007) for sea level pressure, zonal wind,  
182 relative humidity, specific humidity, and temperature; the European Remote Sensing Satellite  
183 Scatterometer (ERS-2) (Bentamy et al., 1999) for surface wind stress; and the Willmott-Matsuura  
184 (Willmott) (Willmott & Matsuura, 1995) data for land surface air temperature.

185 The rainfall mean state is evaluated against the Global Precipitation Climatology Project  
186 (GPCP) monthly product (version 2.1) at a resolution of 2.5° (Adler et al., 2003; Huffman et al.,  
187 2009) while a daily estimate of GPCP version 1.2 at 1° horizontal resolution (GPCP 1DD)  
188 (Huffman et al., 2001, 2012) is used for evaluation of precipitation amount distribution. In addition  
189 to GPCP, the Xie-Arkin pentad observations at 2.5° resolution (Xie and Arkin, 1996) and the  
190 Tropical Rainfall Measuring Mission 3B42 version 7 (TRMM) daily observations at a resolution  
191 of 0.25° over (50°S, 50°N) (Huffman et al., 2007) are applied to evaluate the precipitation variance,  
192 while the latter is also used in the PDF of rainfall intensity and the rainfall amount distribution.  
193 For the rainfall duration evaluation, the TRMM 3B42 v7 3-hourly data is used. To make the  
194 comparison consistent between observations and model simulations, the model data with the same  
195 output frequency to that in the corresponding observations/reanalysis data are used and all  
196 observations/reanalysis data are regridded to the same 1° lat-lon grids as EAMv1.

197

### 198 **3. Results**

#### 199 **3.1. Intraseasonal and synoptic variability**

200 The simulated variability of precipitation is an important aspect of model performance. Here



201 we focus on intraseasonal and synoptic-scale variability. The intraseasonal variability associated  
202 with Madden-Julian oscillations (MJO) is problematic in many GCMs (Jiang et al. 2015; Zhang  
203 and Mu 2005). Figure 1 shows the tropical distribution of the 20-80 day intraseasonal variance for  
204 the total precipitation in observations and simulations. The variance is obtained with a Lanczos  
205 band-pass filter at each grid point. Both Xie-Arkin and TRMM observations show large variance  
206 in the Indian Ocean and western Pacific as well as in the ITCZ and the South Pacific Convergence  
207 Zone (SPCZ) regions. The intraseasonal variance in EAMv1 is much weaker, as in many other  
208 GCMs. Similar to the results in Wang et al. (2016), the STOCH run with the stochastic deep  
209 convection scheme has a significantly enhanced intraseasonal variance in these regions, making it  
210 much more comparable to observations.

211 Besides the intraseasonal variance, the synoptic variance (2-9 day Lanczos band pass-filtered  
212 rainfall anomalies) is also investigated (Fig. 2). The synoptic-scale variance corresponds to  
213 weather activities. In Fig. 2 only TRMM observations are shown to evaluate simulations because  
214 the Xie-Arkin observations are pentad data. In TRMM, the geographical distribution of the  
215 synoptic variance is similar to that of the intraseasonal variance, but with larger amplitudes because  
216 synoptic-scale activities contain much more energy than intraseasonal disturbances. Similar to the  
217 intraseasonal variance, the synoptic variance in the EAMv1 run is also much weaker than that in  
218 observations. The synoptic-scale variance in the STOCH run is about twice as strong as in EAMv1  
219 although it is still underestimated compared to TRMM observations. This result is consistent with  
220 Goswami et al. (2017), which reported enhanced intraseasonal and synoptic variability of  
221 precipitation in the National Centers for Environmental Predictions (NCEP) Climate Forecast  
222 System version 2 (CFSv2) using a stochastic multicloud model parameterization.

223

### 224 **3.2. Rainfall frequency, intensity, amount and duration**

225 Wang et al. (2016) showed that the most significant improvement with the use of the  
226 stochastic deep convection scheme in CAM5 was in the simulated PDF of rainfall intensity over  
227 the tropics, which became very close to TRMM observations. Since there are many modifications  
228 in model configuration and physics parameterizations from CAM5 to EAMv1 (Rasch et al. 2019),  
229 such as a finer vertical resolution, an updated microphysics parameterization (MG2), and the use  
230 of CLUBB in place of separate shallow convection and planetary boundary layer turbulence  
231 parameterizations, it is not clear whether a similar degree of improvement in precipitation intensity  
232 PDF can be achieved with a similar stochastic convection scheme. Using an equal-interval rainfall





233 intensity bin of  $0.5 \text{ mm d}^{-1}$  from 0 to  $200 \text{ mm d}^{-1}$ , Fig. 3 shows the frequencies of the total  
234 precipitation intensity over the tropics ( $20^{\circ}\text{S}$ - $20^{\circ}\text{N}$ ) from TRMM, EAMv1 and STOCH,  
235 respectively. Also shown are the PDFs of large-scale and convective precipitation intensity. As  
236 seen in Fig. 3a, the stochastic convection parameterization in the STOCH run greatly mitigates the  
237 bias of “too much light rain and too little heavy rain”, showing a decrease of the frequency of  
238 rainfall intensity between 1 and  $10 \text{ mm d}^{-1}$  and an increase of that of rainfall intensity larger than  
239  $20 \text{ mm d}^{-1}$  compared to the EAMv1 run. Xie et al. (2019) indicated that the “too much light rain”  
240 in EAMv1 was a result of too frequent convection. Consistent with this notion, Fig. 3b shows that  
241 the reduction of the light rain frequency is entirely from convective precipitation. On the other  
242 hand, the increase of intense precipitation frequency is from both convective and large-scale  
243 precipitation.

244 To understand why the use of stochastic convection scheme decreases the frequency of light  
245 rain and increases the frequency of heavy rain, we conducted an additional simulation. In the  
246 simulation, the setup is identical to the STOCH run except that the ZM scheme is called a second  
247 time at each time step, with input (temperature, moisture, etc.) identical to that for the stochastic  
248 scheme. However, the output is used for diagnostic purposes only and does not participate in model  
249 integration. It is found that (figure not shown) two factors contribute to the decreased frequency  
250 of light rain and increased frequency of heavy rain. First, for a given ensemble mean convective  
251 mass flux (from the ZM scheme) the probability for cloud generation following the Poisson  
252 distribution for a realization in the stochastic scheme can produce more intense precipitation than  
253 obtained by the ZM scheme. Second, the probability distribution results in less frequent convection  
254 in general. This allows the buildup of the atmospheric instability (also see Fig. 9 below in section  
255 3.3), which also leads to heavier convective rainfall (even with ZM scheme alone without  
256 considering the stochastic part) as well as more large-scale condensation. However, we note that  
257 the increase of the frequency in rainfall intensity ranges from  $60$  to  $140 \text{ mm d}^{-1}$  in the STOCH run  
258 is not as much as that in Wang et al. (2016) for CAM5. This will be elucidated through sensitivity  
259 experiments in the next subsection.

260 The frequencies of total precipitation intensity over selected regions also show qualitatively  
261 similar degree of improvement. Fig. 4 shows six regions during their convectively active seasons:  
262 Amazonia, tropical western Pacific, India for June-September, Maritime Continent, Southern  
263 Great Plains (SGP) for May-August and eastern China for June-August in TRMM, EAMv1 and  
264 STOCH, respectively. In all tropical regions, the EAMv1 simulation overestimates the occurrence



265 frequency for precipitation intensities less than  $20 \text{ mm day}^{-1}$  and underestimates it for precipitation  
266 intensities greater than  $20 \text{ mm day}^{-1}$ , similar to the distribution for the entire tropics. In STOCH,  
267 the performance in the pdf over Amazonia and Maritime Continent is better than the pdf over the  
268 entire tropics. Although the biases of “too much light rain” over India and tropical western Pacific  
269 are alleviated by the stochastic deep convection scheme, the bias of “too little heavy rain” remains,  
270 particularly over India where large-scale monsoonal dynamics regulate heavy convective rain  
271 (Wang et al., 2018). For the two midlatitude convection regions (SGP and eastern China), although  
272 there is also noticeable improvement across the precipitation intensity spectrum, it is less  
273 significant compared to other regions, possibly because convection in midlatitude land regions is  
274 not as prevalent as in the tropics.

275 Figure 5 shows the geographical distributions of precipitation frequency for all precipitation,  
276 for precipitation intensities less than  $20 \text{ mm d}^{-1}$ , and more than  $20 \text{ mm d}^{-1}$ , respectively, over the  
277 tropics in observations and simulations (days with precipitation intensity less than  $1 \text{ mm d}^{-1}$  are  
278 considered non-precipitating and thus excluded). In TRMM, the occurrence frequency of rainy  
279 days ranges from 30 to 70% with the most frequent rain along the ITCZ, the SPCZ and in the  
280 Indian Ocean, where the EAMv1 run has as high a frequency as 80-90%, with up to 30% positive  
281 biases. In contrast, the STOCH run reduces the frequency to 50-70% although it is still  
282 overestimated. When the total precipitation is broken down into precipitation rates less than  $20$   
283  $\text{mm d}^{-1}$  and precipitation rate above  $20 \text{ mm d}^{-1}$ , in both observations and simulations the  
284 geographical distribution of the rainy days is dominated by that of days with precipitation intensity  
285 less than  $20 \text{ mm d}^{-1}$ . In comparison with observations, again, the STOCH run reduces the positive  
286 bias of the frequency of precipitation intensity less than  $20 \text{ mm d}^{-1}$  in the EAMv1 run by up to  
287 20%. For precipitation intensities greater than  $20 \text{ mm d}^{-1}$ , the EAMv1 run underestimates their  
288 frequency compared to the TRMM observations. On the other hand, the frequency of occurrence  
289 in the STOCH run is comparable to the TRMM observations.

290 Another metric for the precipitation pdf is the contribution of precipitation within a given  
291 intensity bin to the total precipitation amount. It combines the information of precipitation  
292 frequency distribution and precipitation intensity. While drizzle occurs much more frequently than  
293 the more intense rain events, it may not contribute much to the total precipitation amount.  
294 Following the approach of Kooperman et al. (2016, 2018), we divide the precipitation rate ranging  
295 from  $0.1$  to  $1000 \text{ mm d}^{-1}$  into equal bin intervals on a logarithmic scale, with a bin width of  
296  $\Delta \ln(R) = \Delta R/R = 0.1$ . If the frequency of rainfall rates falling into the  $i$ th bin is denoted  $f_i$ , then



297  $f_i = n_i/N_t$ , where  $N_t$  is the total number of days,  $n_i$  is the number of days with rainfall rates  
 298 falling into the  $i$ th bin. The mean precipitation rate in the  $i$ th bin is then:

299 
$$R_i = \frac{1}{n_i} \sum_{j=1}^{n_i} r_j, \quad (2)$$

300 where  $r_j$  is an individual precipitation rate within the  $i$ th bin. Thus, the contribution to the total  
 301 precipitation amount from the  $i$ th bin per unit bin width is given by:

302 
$$P_i = \frac{f_i R_i}{\Delta \ln(R)} = \frac{1}{\Delta \ln(R)} \frac{1}{N_t} \sum_{j=1}^{n_i} r_j \quad (3)$$

303  $P_i$  has the units of  $\text{mm d}^{-1}$ . The total precipitation amount is then given by:

304 
$$P = \sum_i P_i \Delta \ln(R) = \sum_i f_i R_i \quad (4)$$

305 Accordingly, the amount distributions for total ( $P^T$ ), convective ( $P^C$ ) and large-scale ( $P^L$ ) rainfall  
 306 are given by:

307 
$$P_i^T = \frac{1}{\Delta \ln(R)} \frac{1}{N_t} \sum_{j=1}^{n_i} r_j^T \quad (5)$$

308 
$$P_i^C = \frac{1}{\Delta \ln(R)} \frac{1}{N_t} \sum_{j=1}^{n_i} r_j^C \quad (6)$$

309 
$$P_i^L = \frac{1}{\Delta \ln(R)} \frac{1}{N_t} \sum_{j=1}^{n_i} r_j^L \quad (7)$$

310 where  $r^T$ ,  $r^C$  and  $r^L$  are the total, convective and large-scale rain rates.

311 Figure 6a shows the contribution to the total rainfall amount from each rainfall rate on a  
 312 logarithmic scale for GPCP 1DD, TRMM, and the two simulations, respectively, over the tropics.  
 313 The TRMM observations have larger contributions from intense rainfall rates than GPCP 1DD,  
 314 with the peak contribution rainfall rate of  $28 \text{ mm d}^{-1}$ , higher than the value of  $22 \text{ mm d}^{-1}$  in GPCP  
 315 1DD. The EAMv1 run produces a much smaller peak contribution rainfall rate ( $15 \text{ mm d}^{-1}$ ) than  
 316 the two observations while the STOCH run simulates it realistically ( $23 \text{ mm d}^{-1}$ ), falling in between  
 317 the two observations. Note that precipitation from intensities less than  $1 \text{ mm d}^{-1}$  contributes about  
 318  $0.05 \text{ mm d}^{-1}$  or less to the tropical mean total precipitation, thus justifying treating it as non-  
 319 precipitating in Fig. 5. Fig. 6b shows the convective and large-scale contributions to the simulated  
 320 total precipitation from EAMv1 and STOCH, respectively. The large-scale precipitation shows  
 321 very similar contribution distributions in the two simulations, except for the largest rain rates which  
 322 make only a small contribution to the total. For the most part, large-scale precipitation is not  
 323 affected by how convection is treated in the model, with both simulations having a maximum  
 324 contribution near  $22 \text{ mm d}^{-1}$ . On the other hand, the convective contribution is very different



325 between the two simulations. Similar to the total precipitation, the peak contribution to convective  
326 precipitation is at a much smaller rainfall rate in EAMv1 than in STOCH.

327 Besides precipitation frequency and intensity, another important higher order statistic of  
328 precipitation is the duration of precipitation events; it measures the intermittency of precipitation  
329 (Trenberth et al. 2017). Using 3-hourly data, we calculate the duration of rainfall events as  
330 continuous number of hours of precipitation exceeding a threshold value of  $1 \text{ mm d}^{-1}$ . Figure 7  
331 shows the frequency of precipitation events for different durations over the tropics. 80% of TRMM  
332 observed precipitation events lasts for 3 hours or less, 18% lasts for 6 hours and 2% lasts for 9  
333 hours. In contrast, both EAMv1 and STOCH produce very small proportions ( $\sim 15\%$ ) of  
334 precipitation events that last for 3 hours or less. The frequency of precipitation events lasting 9  
335 hours or longer is extremely overestimated in the model simulations, with some lasting for as long  
336 as 21 hours. This suggests that convection in the model lacks the observed intermittency (Trenberth  
337 et al. 2017) and the use of the stochastic convection scheme does not improve this aspect of the  
338 simulated convection.

339

### 340 **3.3 Sensitivity of rainfall intensity PDF to vertical resolution**

341 A significant modification among several changes in EAMv1 from CAM5 is a much finer  
342 vertical resolution, increasing from 30 levels in CAM5 to 72 levels in EAMv1. Within the PBL  
343 alone EAMv1 has 17 layers compared to 5 layers in CAM5, and the thickness of approximately  
344 20 m for the lowest model layer in EAMv1 is much thinner than that in CAM5, which is 100 m  
345 (Xie et al., 2018). The increased resolution in the PBL in EAMv1 will likely affect the convection  
346 behavior through PBL-convection interactions. In Fig. 3 we showed that the precipitation intensity  
347 pdf is significantly improved with the introduction of the stochastic convection scheme. However,  
348 the improvement was not as striking as that shown in Wang et al. (2016) for CAM5. We suspect  
349 that this is primarily due to the enhanced vertical resolution in EAMv1 rather than other changes  
350 in model physics parameterizations, tunings, or the model dynamic core. To confirm this, EAMv1-  
351 30L and STOCH-30L runs with a vertical resolution of 30 layers are conducted and compared with  
352 the EAMv1 and STOCH runs with the default 72 vertical layers. As seen in Figure 8, when  
353 switching to a configuration of 30 vertical layers, the performance of the STOCH-30L run is very  
354 similar to that in CAM5 (Wang et al., 2016). The frequency distribution of rainfall intensity  
355 between 60 and  $140 \text{ mm d}^{-1}$  almost falls on top of that in TRMM. The PDF of rain intensity in the  
356 EAMv1-30L run is also closer to TRMM observations compared to the EAMv1 run (Fig. 8a). For



357 EAMv1, both convective and large-scale precipitation becomes more intense in the 30-level  
358 configuration. In contrast, the frequency of more intense convective precipitation in STOCH-30L  
359 is increased while that of more intense large-scale precipitation is decreased (Fig. 8b&c), similar  
360 to the dependence of precipitation pdf on horizontal resolution documented in previous studies,  
361 which showed that refining the horizontal resolution should result in more large-scale precipitation  
362 and less convective precipitation (e.g., O'Brien et al., 2016).

363 The causes of sensitivity of convective and large-scale precipitation to vertical resolution are  
364 further examined below. In the ZM convection scheme, the amount of convection is linked to  
365 convective available potential energy (CAPE). Thus, in Figure 9 we present the joint PDF of  
366 convective precipitation and CAPE over the tropics in the four simulations. Note that all parameter  
367 settings are identical between EAMv1 and EAMv1-30L except the vertical resolution. Both  
368 EAMv1 and EAMv1-30L show an approximately linear relationship between CAPE and  
369 convective precipitation. CAPE values are generally smaller in EAMv1-30L than in EAMv1, as  
370 can be seen from the frequency of occurrence of both large and medium CAPE values. However,  
371 the slope of the maximum occurrence frequency is almost twice as large in EAMv1-30L as in  
372 EAMv1 (Fig. 9a&b), giving higher frequency of larger convective precipitation as seen in Fig. 8.  
373 This result is puzzling to us at first. However, note that for a given precipitation rate that the model  
374 produces, there is in general a large range of CAPE values and the CAPE values in EAMv1 are  
375 predominantly larger than in EAMv1-30L as can be seen from the pdf distribution in Fig. 9a and  
376 b. Compared to EAMv1, the smaller CAPE values in EAMv1-30L are caused by higher parcel  
377 launching levels due to thicker model layers near the surface, where the most unstable air is often  
378 found (figure not shown). There is also a bifurcation for medium to large CAPE values. This is  
379 likely related to atmospheric moisture conditions in the atmosphere: for the same CAPE values  
380 there is less precipitation when the atmosphere is dry, and vice versa. With the introduction of the  
381 stochastic deep convection scheme, there are no longer an approximately linear relations between  
382 CAPE and convective precipitation (Fig. 9c&d) in spite of the fact that the CAPE-based closure is  
383 still used to determine the cloud base mass flux (presumably ensemble mean). This is surprising;  
384 it implies that for a given convectively unstable atmospheric thermodynamic condition, the use of  
385 the stochastic scheme often inhibits the triggering of convection, thereby allowing for the buildup  
386 of CAPE for (the less frequently occurring) stronger convection. Similar to EAMv1, smaller  
387 (larger) CAPE values occur more (less) frequently in STOCH-30L due to higher parcel launching  
388 levels. Also, the small and moderate values of CAPE have larger probabilities to precipitate more



389 in STOCH-30L compared to STOCH.

390 Because large-scale precipitation is related to resolved-scale upward moisture flux  $-\omega q/g$ ,  
391 where  $\omega$  is vertical velocity in pressure coordinate,  $q$  is specific humidity and  $g$  is gravitational  
392 acceleration (O'Brien et al., 2016), Fig. 10 shows the PDFs of upward moisture flux at 850 hPa in  
393 the simulations. In comparison with the 72-level configuration, EAMv1-30L has larger frequencies  
394 for upward moisture fluxes larger than  $20 \text{ mm d}^{-1}$  while STOCH-30L has larger frequencies for  
395 upward moisture fluxes from 20 to  $80 \text{ mm d}^{-1}$  but smaller frequencies for fluxes larger than  $80 \text{ mm}$   
396  $\text{d}^{-1}$ . These correspond well with the changes in the PDF of large-scale precipitation from the 30-  
397 level to the 72-level simulations in Fig. 8.

398

### 399 **3.4 Mean state**

400 So far, we have shown that the introduction of a stochastic convection scheme into the E3SM  
401 atmospheric model can significantly improve the simulation of short-term variability and intensity  
402 pdf of precipitation. In climate model development efforts, it is important that an improvement in  
403 some aspects of the model does not lead to degradation of other aspects, at least not to outweigh  
404 the improvement. Thus, it is imperative that we examine the climate mean fields as well. Fig. 11  
405 shows the global distribution of annual mean precipitation in GPCP observations and simulations,  
406 as well as the differences of total, convective, and large-scale precipitation between the STOCH  
407 and EAMv1 runs. Overall, the geographical distributions of precipitation in the two simulations  
408 are similar to those in observations, but both overestimate the tropical precipitation (Fig. 11a-c).  
409 There is a slight increase of rainfall over the tropical western Pacific, equatorial Indian Ocean and  
410 Africa and a slight decrease over India and Amazonia in the STOCH simulation (Fig. 11d). Most  
411 of these changes are from convective precipitation except over equatorial Africa where the changes  
412 are from large-scale precipitation (Fig. 11e&f).

413 The zonal mean of temperature and specific humidity from ERAI and the model biases are  
414 shown in Figure 12. For temperature, EAMv1 produces mostly negative biases in the entire  
415 troposphere over the tropics and subtropics and positive biases in the lower troposphere in high  
416 latitudes. With the stochastic deep convection scheme used, the temperature changes in STOCH  
417 are very minor, increasing slightly from EAMv1. In the simulation of specific humidity, there are  
418 positive biases in the lower troposphere across all latitudes and negative biases above 900 hPa over  
419 the tropics and subtropics in EAMv1. In comparison with EAMv1, the negative biases are  
420 alleviated but the positive biases are increased slightly in STOCH.



421 The overall difference in model performance as measured by the commonly used mean  
422 climate metrics between EAMv1 and STOCH runs is summarized in the Taylor diagram (Fig. 13).  
423 Most metrics are comparable between the two simulations except precipitation, especially over  
424 land where STOCH shows a larger standard deviation than both GPCP and EAMv1. In short, the  
425 mean climate does not change much after the incorporation of the stochastic convection scheme  
426 in EAMv1. This is practically desirable since one does not need to heavily re-tune the model, a  
427 task that is often time-consuming and more of engineering than scientific interest.

428

### 429 **3.5. Response to climate warming**

430 Another aspect of interest concerns the model's response to climate change. It is well known  
431 that the estimated climate sensitivity for future climate projections is sensitive to changes in model  
432 physics parameterizations (Golaz et al. 2019). With the stochastic deep convection  
433 parameterization, it is necessary to check if the response of precipitation and associated extremes  
434 to climate warming differs. As seen in Fig. 14, relative to the current climate simulations, the  
435 geographical patterns and magnitudes of annual mean precipitation changes normalized by the  
436 global-mean surface air warming ( $\Delta T_{sa}$ ) in the +4K SST warming simulations (i.e.,  $(P_{+4k} -$   
437  $P)/P/\Delta T_{sa}$ , units: %/K) with and without the stochastic deep convection scheme are very similar,  
438 both showing maximum increases over the ITCZ, the western Pacific and the Indian Ocean.  
439 Pendergrass et al., (2019) found that the response of extreme precipitation to warming follows a  
440 nonlinear relation:

$$441 \quad \frac{dr_x}{dT_{sa}} = aT_{sa} \quad (8)$$

442 or

$$443 \quad r_x = \frac{1}{2} aT_{sa}^2 + b \quad (9)$$

444 where  $r_x$  is a rainfall extreme index (here using R95p, the total rainfall from the days with daily  
445 rainfall intensity exceeding 95th percentile of the daily precipitation distribution),  $T_{sa}$  is the  
446 global-mean surface air temperature in a warmer world, and  $a$  is the slope of  $dr_x/dT_{sa}$  versus  
447  $T_{sa}$  measuring the strength of the nonlinear response of extreme rainfall to warming. At each grid  
448 point,  $dr_x \approx \Delta r_x$  is equal to R95p in a warmer world minus that under the current climate and  
449 normalized by the global-mean surface air warming ( $dT_{sa} \approx \Delta T_{sa}$ ). With  $T_{sa}$  in the +4K SSTs  
450 warming simulations and the calculated  $dr_x/dT_{sa}$ , the global distributions of the slope,  $a$   
451 (units: %/K<sup>2</sup>), with and without the stochastic deep convection scheme are displayed in Fig. 14c&d.





452 Although the stochastic deep convection parameterization introduces stochasticity into convection  
453 and significantly improves the underestimated frequency of intense precipitation under the current  
454 climate (Wang et al., 2017), it does not lead to a different nonlinear response of precipitation  
455 extremes in a warmer world. Increasing circulation strength as climate warms is considered to be  
456 the main driver for the nonlinear relationship between tropical precipitation extremes and global-  
457 mean surface air temperature (Pendergrass et al., 2019), and it is possible that the circulation  
458 changes with and without the stochastic deep convection scheme are similar. Relative to their  
459 respective current climate states, the responses of the EAMv1-4K and STOCH-4K runs show  
460 similar geographical distributions with comparable maximum nonlinearity over the tropical Pacific  
461 and Atlantic and the Indian Ocean which bears some resemblance to that in Pendergrass et al.  
462 (2019).

463

#### 464 **4. Summary**

465 In this study, we implemented the stochastic deep convection scheme (Plant and Craig, 2008;  
466 Wang et al., 2016) into the DOE EAMv1 and investigated its impact on the simulation of  
467 precipitation. Several improvements are observed with the use of the stochastic convection scheme:  
468 (1) the weak intraseasonal and synoptic-scale variabilities in EAMv1 are enhanced to levels much  
469 closer to those in observations; (2) the “too much light rain and too little heavy rain” bias over the  
470 tropics is significantly alleviated due to less frequent occurrence of drizzling convection and more  
471 frequent occurrence of intense large-scale and convective precipitation contributing to enhanced  
472 heavy rain; (3) the simulated peak precipitation rates (the amount mode) in the precipitation  
473 amount distribution, which contribute the most to the total amount of precipitation, are larger and  
474 are in better agreement with those in TRMM and GPCP observations.

475 While the improvement in the simulated PDF of rainfall intensity is significant, it is less than  
476 what we had expected based on our earlier work with the NCAR CAM5 (Wang et al., 2016). Since  
477 there are many changes from CAM5 to EAMv1, including vertical resolution, model dynamic core  
478 and physics parameterizations, it is not clear which changes are related to the difference in the  
479 improvement of the simulated rainfall pdf. Two sensitivity tests were performed to elucidate this,  
480 both with a coarser vertical resolution configuration of 30 layers (i.e., EAMv1-30L and SOTC-  
481 30L) as in CAM5. The STOCH-30L run successfully reproduces the frequency distribution of  
482 rainfall intensity found by Wang et al. (2016) with an increased frequency of convective  
483 precipitation intensities between 60 and 140 mm d<sup>-1</sup>. This increase is explained by the fact that





484 small and moderate values of CAPE generate more convective precipitation from the altered  
485 relation between them compared to the 72-level configuration due to fewer model layers in the 30-  
486 level resolution. Large-scale precipitation is also influenced by the vertical resolution, but it  
487 behaves differently in EAMv1-30L and STOCH-30L compared with EAMv1 and STOCH  
488 respectively because of the different response of the resolved-scale upward moisture flux at 850  
489 hPa.

490 For any changes in model physics parameterization that improve some aspects of the model  
491 performance, it is important that other aspects are not degraded. It is known in the climate modeling  
492 community that improved intraseasonal variability is often accompanied by a degradation of the  
493 mean state (e.g., Kim et al. 2011; Klingaman and Demott, 2020). We showed that the mean states  
494 in tropospheric temperature, moisture as well as precipitation are not much different with or  
495 without the use of the stochastic convection scheme, and neither are the responses of mean  
496 precipitation and precipitation extremes to climate warming. This is encouraging and desirable for  
497 model development efforts. However, we note that for higher horizontal resolutions (Caldwell et  
498 al., 2019) or a regionally refined mesh version of EAMv1 (Tang et al., 2019), spatial averaging of  
499 the input fields of the stochastic scheme would be needed to make use of convective quasi-  
500 equilibrium over a larger domain. This could be challenging for computational efficiency and it  
501 requires further research in the future.

502

503 **Code and data availability.** The E3SMv1 source code can be downloaded from the E3SM official  
504 website <https://e3sm.org/>. The GPCP 1DD and TRMM 3B42 data are available from NASA GSFC  
505 RSD (<https://psl.noaa.gov/data/gridded/data.gpcp.html>) and Mirador  
506 (<http://mirador.gsfc.nasa.gov>), respectively. The EAMv1 simulation output is provided in an open  
507 repository Zenodo (<http://doi.org/10.5281/zenodo.3902998>).

508

509 **Author contributions.** GJZ conceived the idea. YW developed the model code. YW and WYL  
510 conducted the model simulations. YW performed the analysis. YW and GJZ interpreted the results  
511 and wrote the paper. All authors participated in the revision and editing of the paper.

512

513 **Acknowledgements:** This work is supported by the National Key Research and Development  
514 Program of China Grants 2017YFA0604000, and the National Natural Science Foundation of  
515 China Grants 41975126 and 41605074. GJZ is supported by the Department of Energy, Office of



516 Science, Biological and Environmental Research Program (BER), under Award Numbers DE-  
517 SC0019373 and DE-SC0016504. GCC is supported by subproject A1 of the Transregional  
518 Collaborative Research Center SFB / TRR 165 “Waves to Weather” ([www.wavestoweather.de](http://www.wavestoweather.de))  
519 funded by the German Research Foundation (DFG). Work at LLNL was performed under the  
520 auspices of the U.S. DOE by Lawrence Livermore National Laboratory under contract No. DE-  
521 AC52-07NA27344. SX and QT are supported by the DOE Energy Exascale Earth System Model  
522 (E3SM) project and HYM is funded by the DOE Regional and Global Model Analysis program  
523 area (RGMA) and ASR’s Cloud-Associated Parameterizations Testbed (CAPT) project. This  
524 research used resources of the National Energy Research Scientific Computing Center, a DOE  
525 Office of Science User Facility supported by the Office of Science of the U.S. DOE under Contract  
526 No. DE-AC02-05CH11231.  
527



## 528 **References**

- 529 Adler, R. F., Huffman, G. J., Chang, A., Ferraro, R., Xie, P.-P., Janowiak, J., Rudolf, B., Schneider,  
530 U., Curtis, S., and Bolvin, D.: The version-2 global precipitation climatology project (GPCP)  
531 monthly precipitation analysis (1979–present), *Journal of hydrometeorology*, 4, 1147-1167,  
532 2003.
- 533 Bentamy, A., Queffelec, P., Quilfen, Y., and Katsaros, K.: Ocean surface wind fields estimated  
534 from satellite active and passive microwave instruments, *IEEE transactions on geoscience  
535 and remote sensing*, 37, 2469-2486, 1999.
- 536 Caldwell, P. M., Mamejanov, A., Tang, Q., Van Roekel, L. P., Golaz, J.-C., Lin, W., Bader, D.  
537 C., Keen, N. D., Feng, Y., Jacob, R., Maltrud, M. E., Roberts, A. F., Taylor, M. A., Veneziani,  
538 M., Wang, H., Wolfe, J. D., Balaguru, K., Cameron-Smith, P., Dong, L., Klein, S. A., Leung,  
539 L. R., Li, H.-Y., Li, Q., Liu, X., Neale, R. B., Pinheiro, M., Qian, Y., Ullrich, P. A., Xie, S.,  
540 Yang, Y., Zhang, Y., Zhang, K., and Zhou, T.: The DOE E3SM Coupled Model Version 1:  
541 Description and Results at High Resolution, *Journal of Advances in Modeling Earth Systems*,  
542 11, 4095-4146, 10.1029/2019ms001870, 2019.
- 543 Cohen, B. G., and Craig, G. C.: Fluctuations in an Equilibrium Convective Ensemble. Part II:  
544 Numerical Experiments, *Journal of the Atmospheric Sciences*, 63, 2005-2015,  
545 10.1175/JAS3710.1, 2006.
- 546 Craig, G. C., and Cohen, B. G.: Fluctuations in an Equilibrium Convective Ensemble. Part I:  
547 Theoretical Formulation, *Journal of the Atmospheric Sciences*, 63, 1996-2004,  
548 10.1175/JAS3709.1, 2006.
- 549 Dai, A.: Precipitation Characteristics in Eighteen Coupled Climate Models, *Journal of Climate*, 19,  
550 4605-4630, 10.1175/JCLI3884.1, 2006.
- 551 Davies, L., Jakob, C., May, P., Kumar, V. V., and Xie, S.: Relationships between the large-scale  
552 atmosphere and the small-scale convective state for Darwin, Australia, *Journal of  
553 Geophysical Research: Atmospheres*, 118, 5115-5115, 10.1002/jgrd.50645, 2013.
- 554 Gettelman, A., Morrison, H., Santos, S., Bogenschutz, P., and Caldwell, P.: Advanced two-  
555 moment bulk microphysics for global models. Part II: Global model solutions and aerosol-  
556 cloud interactions, *Journal of Climate*, 28, 1288-1307, 2015.
- 557 Golaz, J.-C., Larson, V. E., and Cotton, W. R.: A PDF-based model for boundary layer clouds.  
558 Part I: Method and model description, *Journal of the atmospheric sciences*, 59, 3540-3551,  
559 2002.



- 560 Golaz, J.-C., Caldwell, P. M., Van Roekel, L. P., Petersen, M. R., Tang, Q., Wolfe, J. D., Abeshu,  
561 G., Anantharaj, V., Asay-Davis, X. S., Bader, D. C., Baldwin, S. A., Bisht, G., Bogenschutz,  
562 P. A., Branstetter, M., Brunke, M. A., Brus, S. R., Burrows, S. M., Cameron-Smith, P. J.,  
563 Donahue, A. S., Deakin, M., Easter, R. C., Evans, K. J., Feng, Y., Flanner, M., Foucar, J. G.,  
564 Fyke, J. G., Griffin, B. M., Hannay, C., Harrop, B. E., Hoffman, M. J., Hunke, E. C., Jacob,  
565 R. L., Jacobsen, D. W., Jeffery, N., Jones, P. W., Keen, N. D., Klein, S. A., Larson, V. E.,  
566 Leung, L. R., Li, H.-Y., Lin, W., Lipscomb, W. H., Ma, P.-L., Mahajan, S., Maltrud, M. E.,  
567 Mامتjanov, A., McClean, J. L., McCoy, R. B., Neale, R. B., Price, S. F., Qian, Y., Rasch,  
568 P. J., Reeves Eyre, J. E. J., Riley, W. J., Ringler, T. D., Roberts, A. F., Roesler, E. L., Salinger,  
569 A. G., Shaheen, Z., Shi, X., Singh, B., Tang, J., Taylor, M. A., Thornton, P. E., Turner, A. K.,  
570 Veneziani, M., Wan, H., Wang, H., Wang, S., Williams, D. N., Wolfram, P. J., Worley, P. H.,  
571 Xie, S., Yang, Y., Yoon, J.-H., Zelinka, M. D., Zender, C. S., Zeng, X., Zhang, C., Zhang, K.,  
572 Zhang, Y., Zheng, X., Zhou, T., and Zhu, Q.: The DOE E3SM Coupled Model Version 1:  
573 Overview and Evaluation at Standard Resolution, *Journal of Advances in Modeling Earth*  
574 *Systems*, 11, 2089-2129, 10.1029/2018ms001603, 2019.
- 575 Goswami, B., Khouider, B., Phani, R., Mukhopadhyay, P., and Majda, A.: Improving synoptic and  
576 intraseasonal variability in CFSv2 via stochastic representation of organized convection,  
577 *Geophysical Research Letters*, 44, 1104-1113, 2017.
- 578 Groenemeijer, P., and Craig, G. C.: Ensemble forecasting with a stochastic convective  
579 parametrization based on equilibrium statistics, *Atmos. Chem. Phys.*, 12, 4555-4565,  
580 10.5194/acp-12-4555-2012, 2012.
- 581 Hsu, J., and Prather, M. J.: Stratospheric variability and tropospheric ozone, *Journal of*  
582 *Geophysical Research: Atmospheres*, 114, 2009.
- 583 Huffman, G. J., Adler, R. F., Morrissey, M. M., Bolvin, D. T., Curtis, S., Joyce, R., McGavock,  
584 B., and Susskind, J.: Global precipitation at one-degree daily resolution from multisatellite  
585 observations, *Journal of hydrometeorology*, 2, 36-50, 2001.
- 586 Huffman, G. J., Bolvin, D. T., Nelkin, E. J., Wolff, D. B., Adler, R. F., Gu, G., Hong, Y., Bowman,  
587 K. P., and Stocker, E. F.: The TRMM multisatellite precipitation analysis (TMPA): Quasi-  
588 global, multiyear, combined-sensor precipitation estimates at fine scales, *Journal of*  
589 *hydrometeorology*, 8, 38-55, 2007.
- 590 Huffman, G., Bolvin, D., and Adler, R.: GPCP version 1.2 1-degree daily (1DD) precipitation data  
591 set, World Data Center A, National Climatic Data Center, Asheville, NC [Available at



- 592 <ftp://rsd.gsfc.nasa.gov/pub/1dd-v1.2/>, 2012.
- 593 Jones, T. R., and Randall, D. A.: Quantifying the limits of convective parameterizations, *Journal*  
594 *of Geophysical Research: Atmospheres*, 116, 10.1029/2010jd014913, 2011.
- 595 Kain, J. S., and Fritsch, J. M.: A One-Dimensional Entraining/Detraining Plume Model and Its  
596 Application in Convective Parameterization, *Journal of the Atmospheric Sciences*, 47, 2784-  
597 2802, 10.1175/1520-0469(1990)047<2784:AODEPM>2.0.CO;2, 1990.
- 598 Kain, J. S.: The Kain–Fritsch Convective Parameterization: An Update, *Journal of Applied*  
599 *Meteorology*, 43, 170-181, 10.1175/1520-0450(2004)043<0170:TKCPAU>2.0.CO;2, 2004.
- 600 Keane, R. J., Craig, G. C., Keil, C., and Zängl, G.: The Plant–Craig Stochastic Convection Scheme  
601 in ICON and Its Scale Adaptivity, *Journal of the Atmospheric Sciences*, 71, 3404-3415,  
602 10.1175/JAS-D-13-0331.1, 2014.
- 603 Keane, R. J., Plant, R. S., and Tennant, W. J.: Evaluation of the Plant–Craig stochastic convection  
604 scheme (v2. 0) in the ensemble forecasting system MOGREPS-R (24 km) based on the  
605 Unified Model (v7. 3), *Geoscientific Model Development*, 9, 1921-1935, 2016.
- 606 Khouider, B., Biello, J., and Majda, A. J.: A stochastic multicloud model for tropical convection,  
607 187-216, 2010.
- 608 Kim, D., Sobel, A. H., Maloney, E. D., Frierson, D. M., and Kang, I.-S.: A systematic relationship  
609 between intraseasonal variability and mean state bias in AGCM simulations, *Journal of*  
610 *Climate*, 24, 5506-5520, 2011.
- 611 Klingaman, N. P., and Demott, C. A.: Mean State Biases and Interannual Variability Affect  
612 Perceived Sensitivities of the Madden-Julian Oscillation to Air-Sea Coupling, *Journal of*  
613 *Advances in Modeling Earth Systems*, 12, e2019MS001799, 10.1029/2019ms001799, 2020.
- 614 Kooperman, G. J., Pritchard, M. S., Burt, M. A., Branson, M. D., and Randall, D. A.: Robust  
615 effects of cloud superparameterization on simulated daily rainfall intensity statistics across  
616 multiple versions of the Community Earth System Model, *Journal of Advances in Modeling*  
617 *Earth Systems*, 8, 140-165, 2016.
- 618 Kooperman, G. J., Pritchard, M. S., O'Brien, T. A., and Timmermans, B. W.: Rainfall From  
619 Resolved Rather Than Parameterized Processes Better Represents the Present - Day and  
620 Climate Change Response of Moderate Rates in the Community Atmosphere Model, *Journal*  
621 *of advances in modeling earth systems*, 10, 971-988, 2018.
- 622 Larson, V. E., and Golaz, J.-C.: Using probability density functions to derive consistent closure  
623 relationships among higher-order moments, *Monthly Weather Review*, 133, 1023-1042, 2005.



- 624 Lin, J. W. B., and Neelin, J. D.: Influence of a stochastic moist convective parameterization on  
625 tropical climate variability, *Geophysical research letters*, 27, 3691-3694, 2000.
- 626 Lin, J. W.-B., and Neelin, J. D.: Considerations for stochastic convective parameterization, *Journal*  
627 *of the atmospheric sciences*, 59, 959-975, 2002.
- 628 Liu, X., Ma, P.-L., Wang, H., Tilmes, S., Singh, B., Easter, R., Ghan, S., and Rasch, P.: Description  
629 and evaluation of a new four-mode version of the Modal Aerosol Module (MAM4) within  
630 version 5.3 of the Community Atmosphere Model, *Geoscientific Model Development*  
631 (Online), 9, 2016.
- 632 Loeb, N. G., Wielicki, B. A., Doelling, D. R., Smith, G. L., Keyes, D. F., Kato, S., Manalo-Smith,  
633 N., and Wong, T.: Toward optimal closure of the Earth's top-of-atmosphere radiation budget,  
634 *Journal of Climate*, 22, 748-766, 2009.
- 635 McLinden, C., Olsen, S., Hannegan, B., Wild, O., Prather, M., and Sundet, J.: Stratospheric ozone  
636 in 3 - D models: A simple chemistry and the cross - tropopause flux, *Journal of Geophysical*  
637 *Research: Atmospheres*, 105, 14653-14665, 2000.
- 638 Morrison, H., and Gettelman, A.: A New Two-Moment Bulk Stratiform Cloud Microphysics  
639 Scheme in the Community Atmosphere Model, Version 3 (CAM3). Part I: Description and  
640 Numerical Tests, *Journal of Climate*, 21, 3642-3659, 10.1175/2008JCLI2105.1, 2008.
- 641 O'Brien, T. A., Collins, W. D., Kashinath, K., Rübél, O., Byna, S., Gu, J., Krishnan, H., and Ullrich,  
642 P. A.: Resolution dependence of precipitation statistical fidelity in hindcast simulations,  
643 *Journal of Advances in Modeling Earth Systems*, 8, 976-990, 2016.
- 644 O'Gorman, P. A., and Schneider, T.: The physical basis for increases in precipitation extremes in  
645 simulations of 21st-century climate change, *Proceedings of the National Academy of*  
646 *Sciences of the United States of America*, 106, 14773-14777, 2009.
- 647 Palmer, T. N.: A nonlinear dynamical perspective on model error: A proposal for non - local  
648 stochastic - dynamic parametrization in weather and climate prediction models, *Quarterly*  
649 *Journal of the Royal Meteorological Society*, 127, 279-304, 2001.
- 650 Palmer, T. N.: Towards the probabilistic Earth-system simulator: a vision for the future of climate  
651 and weather prediction†, *Quarterly Journal of the Royal Meteorological Society*, 138, 841-  
652 861, 2012.
- 653 Pendergrass, A., Coleman, D., Deser, C., Lehner, F., Rosenbloom, N., and Simpson, I.: Nonlinear  
654 response of extreme precipitation to warming in CESM1, *Geophysical Research Letters*, 46,  
655 10551-10560, 2019.



- 656 Peters, K., Jakob, C., Davies, L., Khouider, B., and Majda, A. J.: Stochastic Behavior of Tropical  
657 Convection in Observations and a Multicloud Model, *Journal of the Atmospheric Sciences*,  
658 70, 3556-3575, 2013.
- 659 Peters, K., Crueger, T., Jakob, C., and Mobis, B.: Improved MJO - simulation in ECHAM6.3 by  
660 coupling a Stochastic Multicloud Model to the convection scheme, *Journal of Advances in*  
661 *Modeling Earth Systems*, 9, 193-219, 2017.
- 662 Plant, R. S., and Craig, G. C.: A Stochastic Parameterization for Deep Convection Based on  
663 Equilibrium Statistics, *Journal of the Atmospheric Sciences*, 65, 87-105,  
664 10.1175/2007JAS2263.1, 2008.
- 665 Rasch, P., Xie, S., Ma, P. L., Lin, W., Wang, H., Tang, Q., Burrows, S., Caldwell, P., Zhang, K.,  
666 and Easter, R.: An overview of the atmospheric component of the Energy Exascale Earth  
667 System Model, *Journal of Advances in Modeling Earth Systems*, 11, 2377-2411, 2019.
- 668 Sakradzija, M., Seifert, A., and Heus, T.: Fluctuations in a quasi-stationary shallow cumulus cloud  
669 ensemble, *Nonlin. Processes Geophys.*, 22, 65-85, 10.5194/npg-22-65-2015, 2015.
- 670 Simmons, A., Uppala, S., Dee, D., and Kobayashi, S.: ERA-Interim: New ECMWF reanalysis  
671 products from 1989 onwards, *ECMWF Newsl.*, 110, 1–11, 2007.
- 672 Stone, D., Risser, M. D., Angelil, O., Wehner, M., Cholia, S., Keen, N., Krishnan, H., O'Brien, T.  
673 A., and Collins, W. D.: A basis set for exploration of sensitivity to prescribed ocean conditions  
674 for estimating human contributions to extreme weather in CAM5.1-1degree, *Weather and*  
675 *climate extremes*, 19, 10-19, 2018.
- 676 Tang, Q., Klein, S. A., Xie, S., Lin, W., Golaz, J.-C., Roesler, E. L., Taylor, M. A., Rasch, P. J.,  
677 Bader, D. C., and Berg, L. K.: Regionally refined test bed in E3SM atmosphere model version  
678 1 (EAMv1) and applications for high-resolution modeling, *Geoscientific Model Development*  
679 (Online), 12, 2019.
- 680 Trenberth, K. E., Zhang, Y., and Gehne, M.: Intermittency in Precipitation: Duration, Frequency,  
681 Intensity, and Amounts Using Hourly Data, *Journal of Hydrometeorology*, 18, 1393-1412,  
682 10.1175/jhm-d-16-0263.1, 2017.
- 683 Wang, Y., Liu, X., Hoose, C., and Wang, B.: Different contact angle distributions for  
684 heterogeneous ice nucleation in the Community Atmospheric Model version 5, *Atmospheric*  
685 *Chemistry and Physics*, 10411, 2014.
- 686 Wang, Y., and Zhang, G. J.: Global climate impacts of stochastic deep convection parameterization  
687 in the NCAR CAM5, *Journal of Advances in Modeling Earth Systems*, 8, 1641-1656,





- 688 doi:10.1002/2016MS000756, 2016.
- 689 Wang, Y., Zhang, G. J., and Craig, G. C.: Stochastic convective parameterization improving the  
690 simulation of tropical precipitation variability in the NCAR CAM5, *Geophysical Research*  
691 *Letters*, 43, 6612-6619, doi:10.1002/2016GL069818, 2016.
- 692 Wang, Y., Zhang, G. J., and Jiang, Y.: Linking Stochasticity of Convection to Large-Scale Vertical  
693 Velocity to Improve Indian Summer Monsoon Simulation in the NCAR CAM5, *Journal of*  
694 *Climate*, 31, 6985-7002, 10.1175/jcli-d-17-0785.1, 2018.
- 695 Watson, P. A. G., Berner, J., Corti, S., Davini, P., Von Hardenberg, J., Sanchez, C., Weisheimer,  
696 A., and Palmer, T. N.: The impact of stochastic physics on tropical rainfall variability in  
697 global climate models on daily to weekly time scales, *Journal of Geophysical Research*, 122,  
698 5738-5762, 2017.
- 699 Webb, M. J., Andrews, T., Bodas-Salcedo, A., Bony, S., Bretherton, C. S., Chadwick, R., Chepfer,  
700 H., Douville, H., Good, P., and Kay, J. E.: The cloud feedback model intercomparison project  
701 (CFMIP) contribution to CMIP6, *Geoscientific Model Development*, 2017, 359-384, 2017.
- 702 Willmott, C. J., and Matsuura, K.: Smart interpolation of annually averaged air temperature in the  
703 United States, *Journal of Applied Meteorology*, 34, 2577-2586, 1995.
- 704 Xie, P., and Arkin, P. A.: Analyses of Global Monthly Precipitation Using Gauge Observations,  
705 Satellite Estimates, and Numerical Model Predictions, *Journal of Climate*, 9, 840-858,  
706 10.1175/1520-0442(1996)009<0840:AOGMPU>2.0.CO;2, 1996.
- 707 Xie, S., Lin, W., Rasch, P. J., Ma, P. L., Neale, R., Larson, V. E., Qian, Y., Bogenschutz, P. A.,  
708 Caldwell, P., and Cameron - Smith, P.: Understanding cloud and convective characteristics  
709 in version 1 of the E3SM atmosphere model, *Journal of Advances in Modeling Earth Systems*,  
710 10, 2618-2644, 2018.
- 711 Xie, S., Wang, Y., Lin, W., Ma, H., Tang, Q., Tang, S., Zheng, X., Golaz, J., Zhang, G. J., and  
712 Zhang, M.: Improved Diurnal Cycle of Precipitation in E3SM With a Revised Convective  
713 Triggering Function, *Journal of Advances in Modeling Earth Systems*, 11, 2290-2310, 2019.
- 714 Zhang, G. J., and Mu, M.: Simulation of the Madden-Julian Oscillation in the NCAR CCM3 Using  
715 a Revised Zhang-McFarlane Convection Parameterization Scheme, *Journal of Climate*, 18,  
716 4046-4064, 2005a.
- 717 Zhang, G. J., and Mu, M.: Effects of modifications to the Zhang-McFarlane convection  
718 parameterization on the simulation of the tropical precipitation in the National Center for  
719 Atmospheric Research Community Climate Model, version 3, *Journal of Geophysical*





- 720 Research: Atmospheres, 110, D09109, 10.1029/2004JD005617, 2005b.
- 721 Zhang, G. J., Song, X., and Wang, Y.: The double ITCZ syndrome in GCMs: A coupled feedback  
722 problem among convection, clouds, atmospheric and ocean circulations, Atmospheric  
723 Research, 2019.
- 724 Zhang, G. J., and Wang, H.: Toward mitigating the double ITCZ problem in NCAR CCSM3,  
725 Geophysical Research Letters, 33, 2006.
- 726 Zhang, Y., Xie, S., Lin, W., Klein, S. A., Zelinka, M., Ma, P. L., Rasch, P. J., Qian, Y., Tang, Q.,  
727 and Ma, H. Y.: Evaluation of clouds in version 1 of the E3SM atmosphere model with satellite  
728 simulators, Journal of Advances in Modeling Earth Systems, 11, 1253-1268, 2019.
- 729



730 **Table captions**

731 Table 1. List of simulations.

732



733 **Table 1.** List of simulations.

Simulation	Years	Vertical Levels	Description
EAMv1	6	72	Standard EAMv1 with the default deterministic ZM deep convection scheme for simulating the current climate <sup>1</sup>
STOCH	6	72	Same as EAMv1, but coupling with the PC stochastic deep convection scheme with the deterministic ZM deep convection scheme
EAMv1-30L	6	30	Same as EAMv1, but using a vertical resolution configuration of 30 layers
STOCH-30L	6	30	Same as STOCH, but using a vertical resolution configuration of 30 layers
EAMv1-4K	3	72	Same as EAMv1, but for simulating a warmer world <sup>2</sup>
STOCH-4K	3	72	Same as STOCH, but for simulating a warmer world

734 <sup>1</sup>Atmosphere-only simulations, using fully prognostic atmosphere and land models with prescribed,  
735 seasonally varying climatological present-day sea surface temperatures (SSTs) and sea ice extent,  
736 recycled yearly.

737 <sup>2</sup>For simulating a warmer world, the atmosphere-only simulations are subjected to a composite  
738 SST warming pattern derived from the Coupled Model Intercomparison Project Phase 3 (CMIP3)  
739 coupled models.

740



741 **Figure captions**

742 **Figure 1.** Spatial distributions of the 20–80 day variance of rainfall from (a) the Xie-Arkin  
743 observations, (b) TRMM, (c) EAMv1, and (d) STOCH, respectively (units:  $\text{mm}^2 \text{d}^{-2}$ ).

744 **Figure 2.** Spatial distributions of the synoptic variance of rainfall from (a) TRMM, (b) EAMv1,  
745 and (c) STOCH, respectively (units:  $\text{mm}^2 \text{d}^{-2}$ ).

746 **Figure 3.** Frequency distributions of (a) total (solid line), (b) convective (solid line) and large-  
747 scale (dashed line) precipitation intensity over the tropics ( $20^\circ\text{S}$ ,  $20^\circ\text{N}$ ) for EAMv1 (blue) and  
748 STOCH (red) respectively. For total precipitation, the TRMM observations (black) are included  
749 for evaluation.

750 **Figure 4.** Frequency distributions of total precipitation intensity over Amazon ( $20^\circ\text{S}$ – $5^\circ\text{N}$ ,  $40^\circ\text{W}$ –  
751  $80^\circ\text{W}$ ), tropical western Pacific (TWP) ( $0^\circ\text{N}$ – $15^\circ\text{N}$ ,  $130^\circ\text{E}$ – $170^\circ\text{E}$ ), India ( $14^\circ\text{N}$ – $26.5^\circ\text{N}$ ,  $74.5^\circ\text{E}$ –  
752  $94^\circ\text{E}$ ; for June–September), Maritime Continent (MC) ( $10^\circ\text{S}$ – $10^\circ\text{N}$ ,  $90^\circ\text{E}$ – $160^\circ\text{E}$ ), Southern Great  
753 Plains (SGP) ( $37^\circ\text{N}$ – $42^\circ\text{N}$ ,  $90^\circ\text{W}$ – $110^\circ\text{W}$ ; for May–August) and eastern China ( $25^\circ\text{N}$ – $35^\circ\text{N}$ ,  $100^\circ\text{E}$ –  
754  $120^\circ\text{E}$ ; for June–August) for TRMM (black), EAMv1 (blue) and STOCH (red) respectively.

755 **Figure 5.** Spatial distributions of frequencies of total rainfall intensity larger than (top row)  $1 \text{ mm}$   
756  $\text{d}^{-1}$ , (middle row) between  $1$  and  $20 \text{ mm d}^{-1}$  and (bottom row) larger than  $20 \text{ mm d}^{-1}$  for TRMM,  
757 EAMv1 and STOCH, respectively.

758 **Figure 6.** Annual mean rainfall amount distributions of (a) total precipitation (solid line) over the  
759 tropics ( $20^\circ\text{S}$ ,  $20^\circ\text{N}$ ) for GPCP 1DD (grey), TRMM (black), EAMv1 (blue) and STOCH (red),  
760 respectively. Individual distributions of (b) convective (solid line) and large-scale (dashed line)  
761 precipitation in EAMv1 (blue) and STOCH (red) are also shown. The rainfall intensity on the x-  
762 axis is on a logarithmic scale with bin intervals of  $\Delta \ln(R) = \Delta R/R = 0.1$ .

763 **Figure 7.** Histogram of percentage frequency of total rainy events as a function of their duration  
764 using 3-hourly data (conditional probability of rainfall, given rainfall the previous times) from  
765 TRMM (black), EAMv1 (blue) and STOCH (red) for the threshold rainfall rate of  $1 \text{ mm d}^{-1}$  over  
766 the tropics.

767 **Figure 8.** Same as Fig. 3, but including PDFs for EAMv1-30L and STOCH-30L (both dashed  
768 lines).

769 **Figure 9.** Joint PDFs of CAPE versus convective precipitation over the tropics ( $20^\circ\text{S}$ ,  $20^\circ\text{N}$ ) from  
770 (a) EAMv1, (b) EAMv1-30L, (c) STOCH, and (d) STOCH-30L, respectively.

771 **Figure 10.** Frequencies of the resolved upward moisture flux over the tropics ( $20^\circ\text{S}$ ,  $20^\circ\text{N}$ ) in  
772 EAMv1, EAMv1-30L, STOCH and STOCH-30L, respectively.



773 **Figure 11.** Global distributions of total precipitation for (a) GPCP, (b) EAMv1, and (c) STOCH,  
774 and differences of (d) total, (e) convective and (f) large-scale precipitation between STOCH and  
775 EAMv1. Differences with a confidence level greater than 95% in (d-f) are stippled.

776 **Figure 12.** Annual and zonal mean cross sections of (a-c) temperature and (d-f) specific humidity  
777 for (a&d) ERAI and differences for (b&e) EAMv1-ERAI and (c&f) STOCH-EAMv1. Differences  
778 with a confidence level greater than 95% in between STOCH and EAMv1 are stippled.

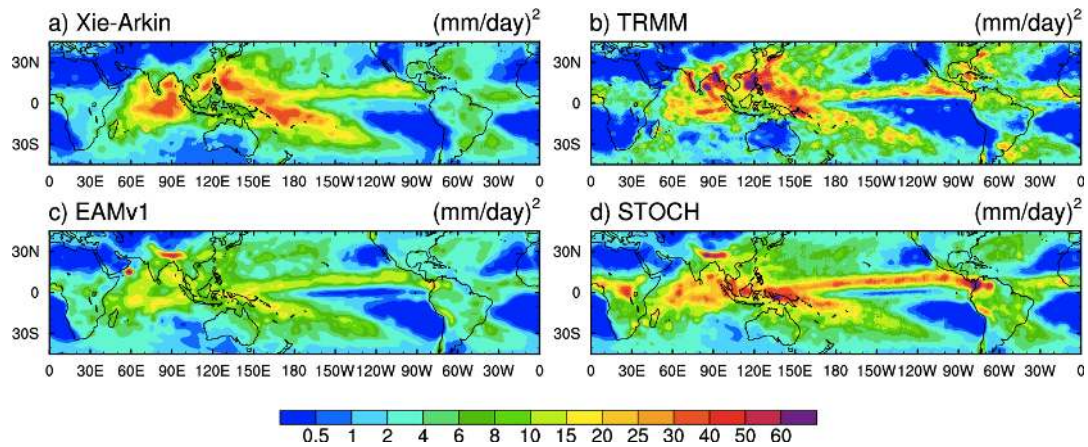
779 **Figure 13.** Taylor diagram with metrics for STOCH, compared with EAMv1.

780 **Figure 14.** Geographical distributions of responses of (a&b) annual mean precipitation and (c&d)  
781 precipitation extremes (R95p) to climate warming from +4K experiments. Differences with a  
782 confidence level greater than 95% are stippled.

783



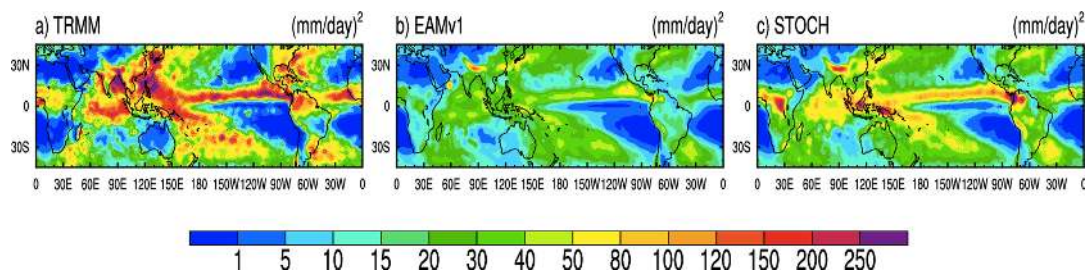
784 **Figures**



785

786 **Figure 1.** Spatial distributions of the 20–80 day variance of rainfall from (a) the Xie-Arkin  
787 observations, (b) TRMM, (c) EAMv1, and (d) STOCH, respectively (units:  $\text{mm}^2 \text{d}^{-2}$ ).

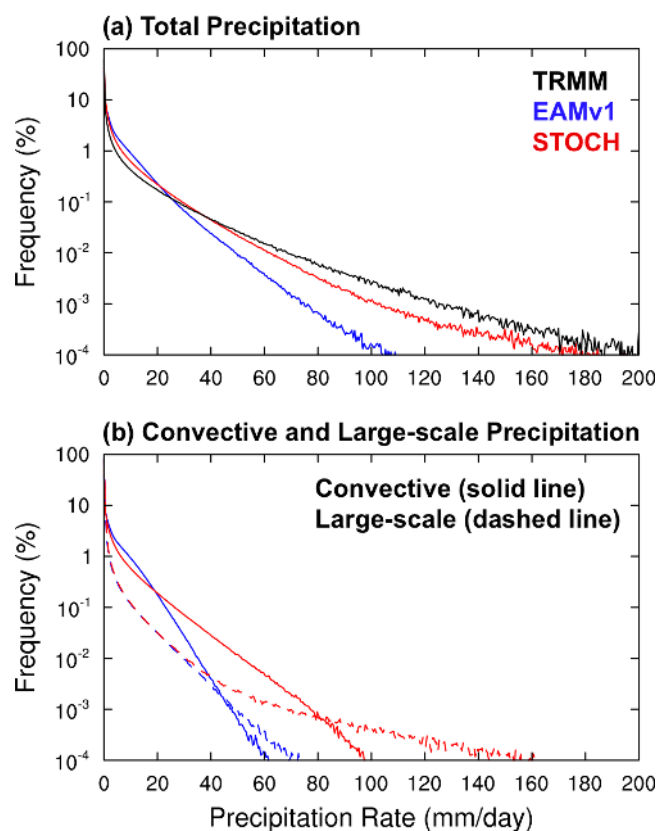
788



789

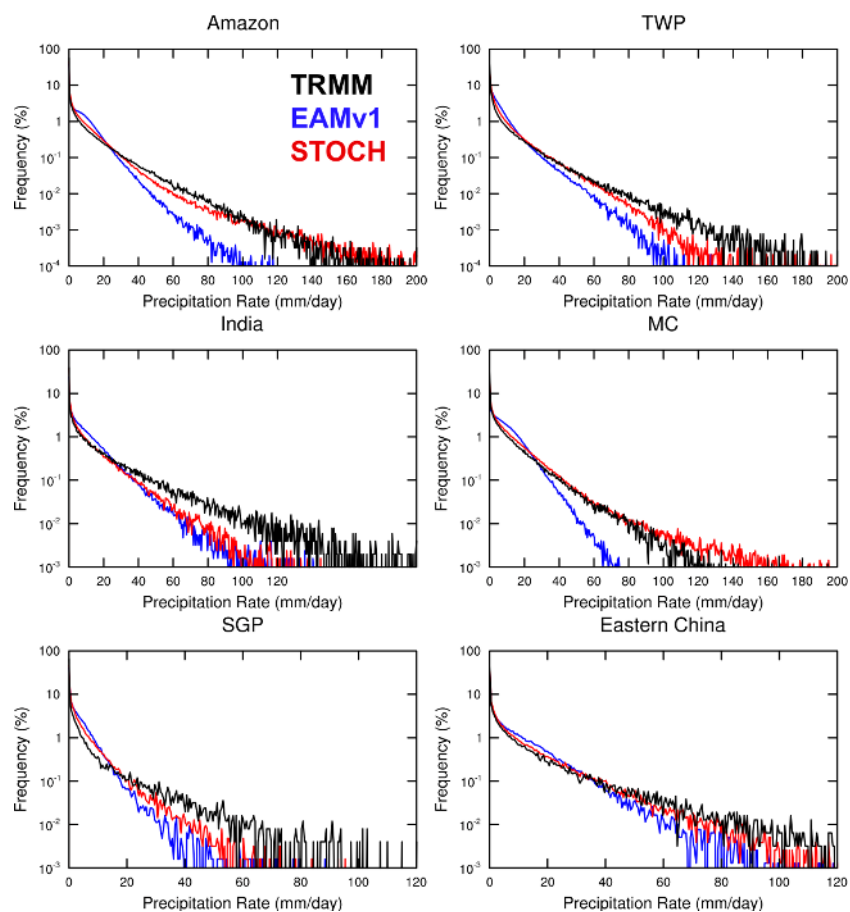
790 **Figure 2.** Spatial distributions of the synoptic variance of rainfall from (a) TRMM, (b) EAMv1,  
791 and (c) STOCH, respectively (units:  $\text{mm}^2 \text{d}^{-2}$ ).

792



793  
794 **Figure 3.** Frequency distributions of (a) total (solid line), (b) convective (solid line) and large-  
795 scale (dashed line) precipitation intensity over the tropics (20°S, 20°N) for EAMv1 (blue) and  
796 STOCH (red) respectively. For total precipitation, the TRMM observations (black) are included  
797 for evaluation.  
798

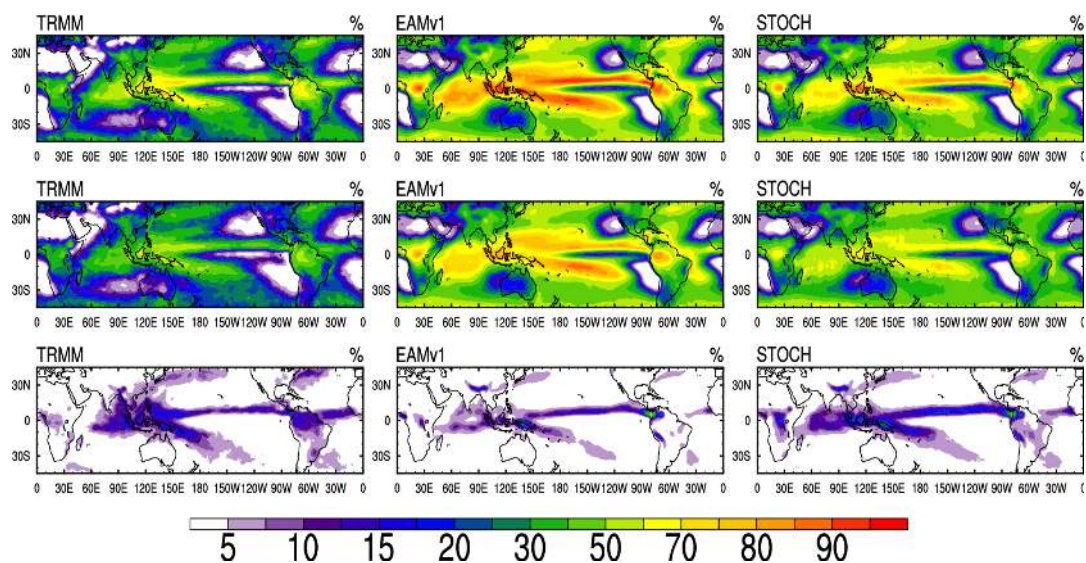




799

800 **Figure 4.** Frequency distributions of total precipitation intensity over Amazon (20°S-5°N, 40°W-  
801 80°W), tropical western Pacific (TWP) (0°N-15°N, 130°E-170°E), India (14°N-26.5°N, 74.5°E-  
802 94°E; for June-September), Maritime Continent (MC) (10°S-10°N, 90°E-160°E), Southern Great  
803 Plains (SGP) (37°N-42°N, 90°W-110°W; for May-August) and eastern China (25°N-35°N, 100°E-  
804 120°E; for June-August) for TRMM (black), EAMv1 (blue) and STOCH (red) respectively.

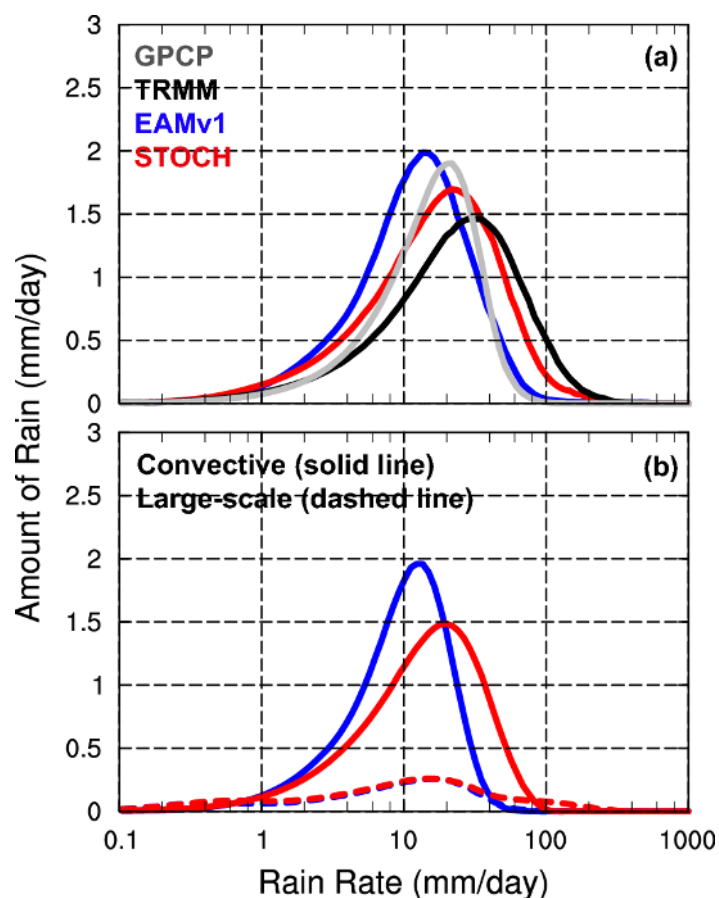
805



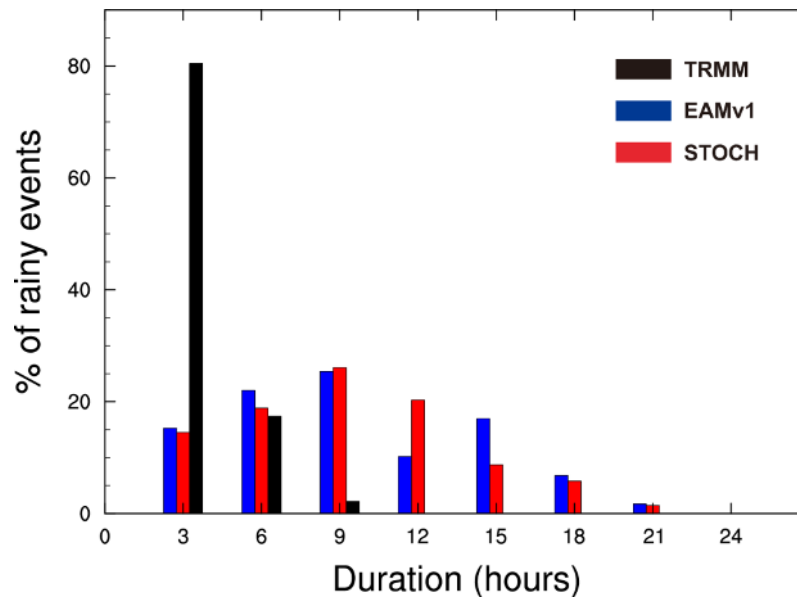
806

807 **Figure 5.** Spatial distributions of frequencies of total rainfall intensity larger than (top row) 1 mm  
808  $\text{d}^{-1}$ , (middle row) between 1 and 20  $\text{mm d}^{-1}$  and (bottom row) larger than 20  $\text{mm d}^{-1}$  for TRMM,  
809 EAMv1 and STOCH, respectively.

810



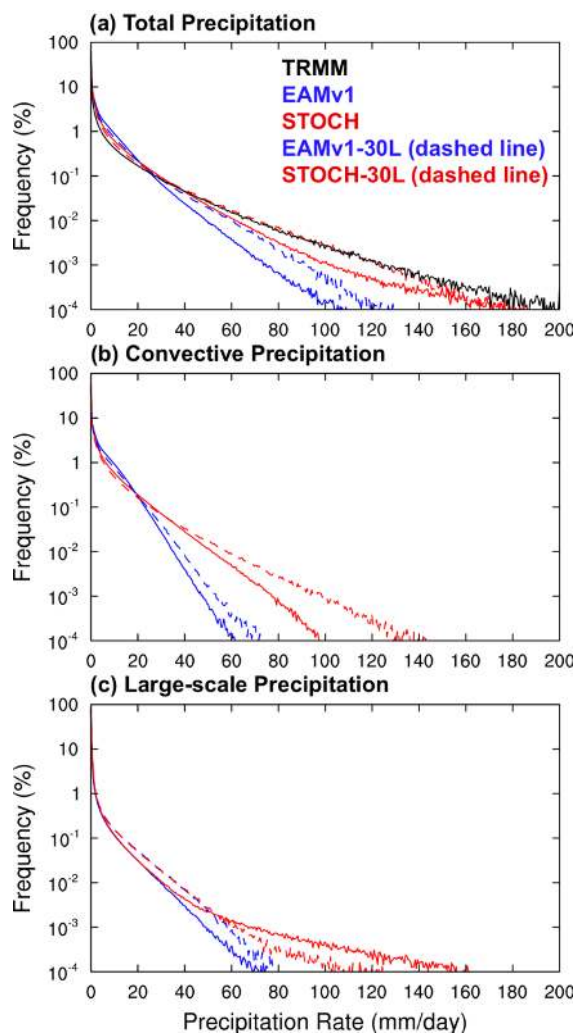
811  
812 **Figure 6.** Annual mean rainfall amount distributions of (a) total precipitation (solid line) over the  
813 tropics (20°S, 20°N) for GPCP 1DD (grey), TRMM (black), EAMv1 (blue) and STOCH (red),  
814 respectively. Individual distributions of (b) convective (solid line) and large-scale (dashed line)  
815 precipitation in EAMv1 (blue) and STOCH (red) are also shown. The rainfall intensity on the x-  
816 axis is on a logarithmic scale with bin intervals of  $\Delta \ln(R) = \Delta R/R = 0.1$ .  
817



818

819 **Figure 7.** Histograms of percentage frequency of total rainy events as a function of their duration  
820 using 3-hourly data (conditional probability of rainfall, given rainfall the previous times) from  
821 TRMM (black), EAMv1 (blue) and STOCH (red) for the threshold rainfall rate of  $1 \text{ mm d}^{-1}$  over  
822 the tropics.

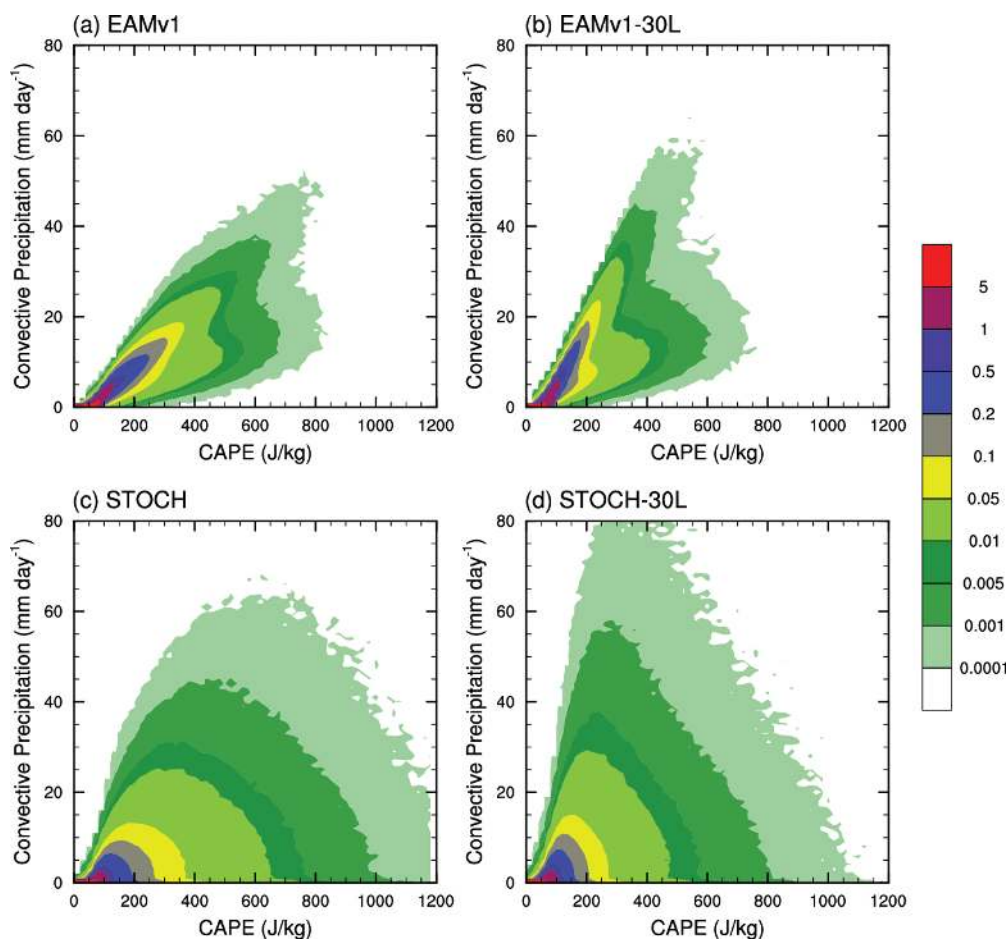
823



824

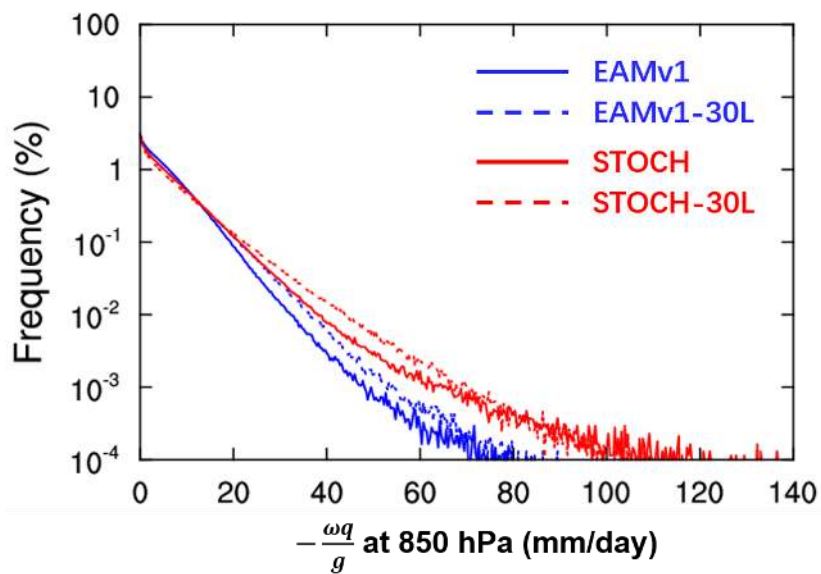
825 **Figure 8.** Same as Fig. 3, but including PDFs for EAMv1-30L and STOCH-30L (both dashed  
826 lines).

827



828  
829  
830  
831

**Figure 9.** Joint PDFs of CAPE versus convective precipitation over the tropics (20°S, 20°N) from (a) EAMv1, (b) EAMv1-30L, (c) STOCH, and (d) STOCH-30L, respectively.

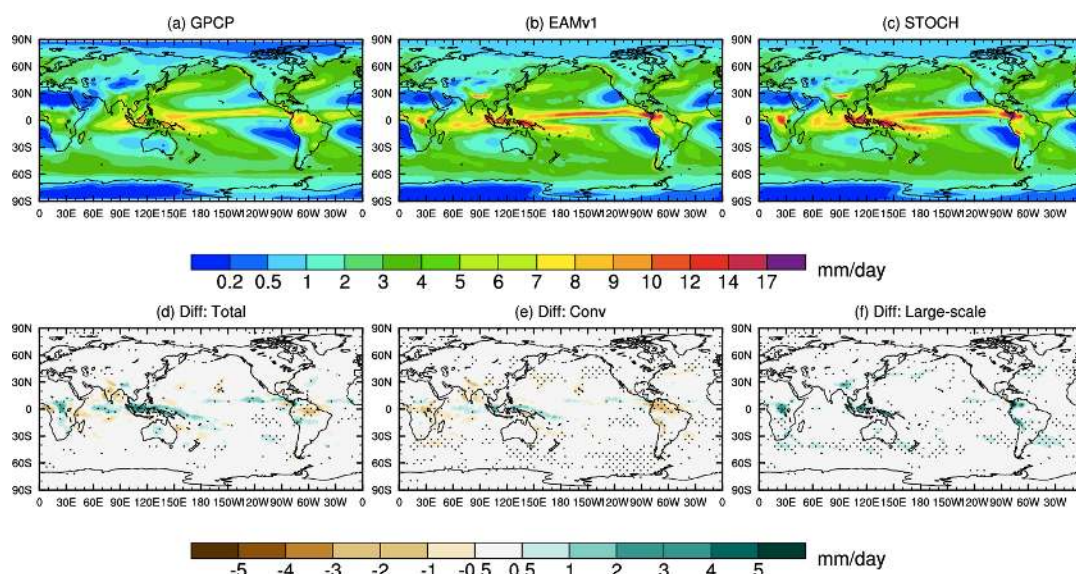


832

833 **Figure 10.** Frequencies of the resolved upward moisture flux over the tropics (20°S, 20°N) in  
834 EAMv1, EAMv1-30L, STOCH and STOCH-30L, respectively.

835

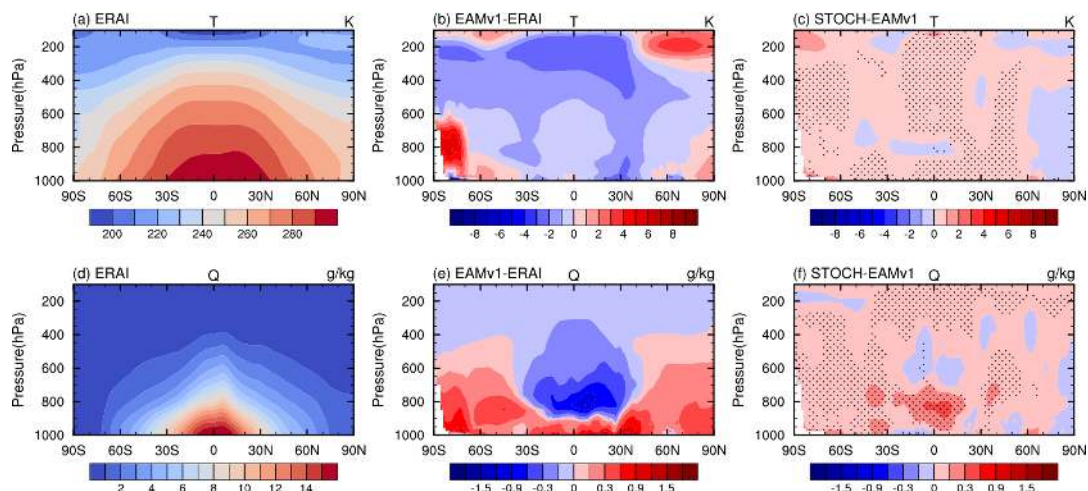




836  
837  
838  
839  
840

**Figure 11.** Global distributions of total precipitation for (a) GPCP, (b) EAMv1, and (c) STOCH, and differences of (d) total, (e) convective and (f) large-scale precipitation between STOCH and EAMv1. Differences with a confidence level greater than 95% in (d-f) are stippled.

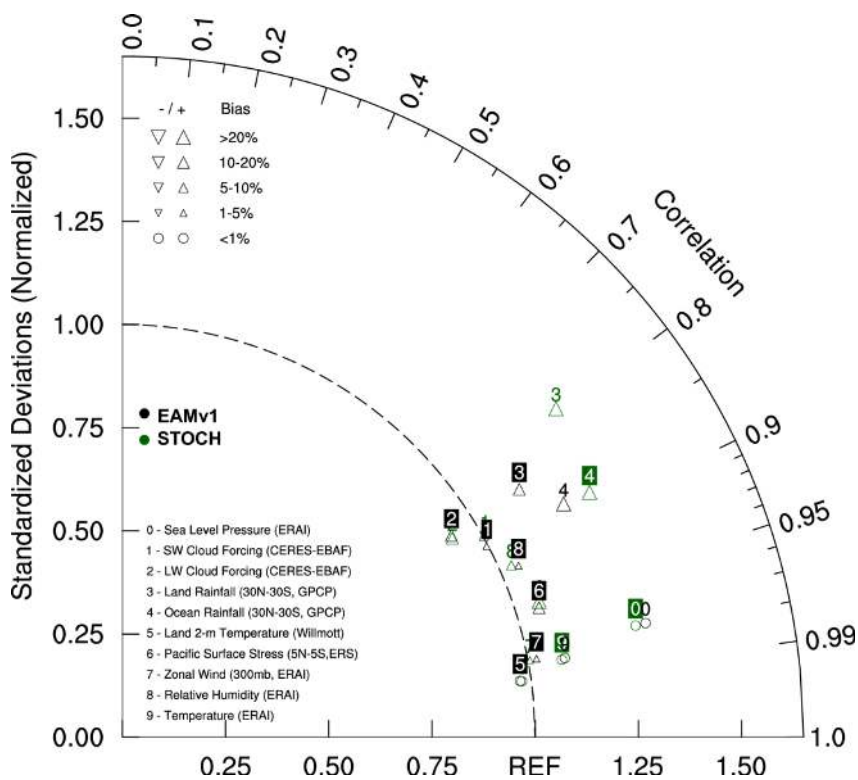




841

842 **Figure 12.** Annual and zonal mean cross sections of (a-c) temperature and (d-f) specific humidity  
843 for (a&d) ERAI and differences for (b&e) EAMv1-ERAI and (c&f) STOCH-EAMv1. Differences  
844 with a confidence level greater than 95% in between STOCH and EAMv1 are stippled.

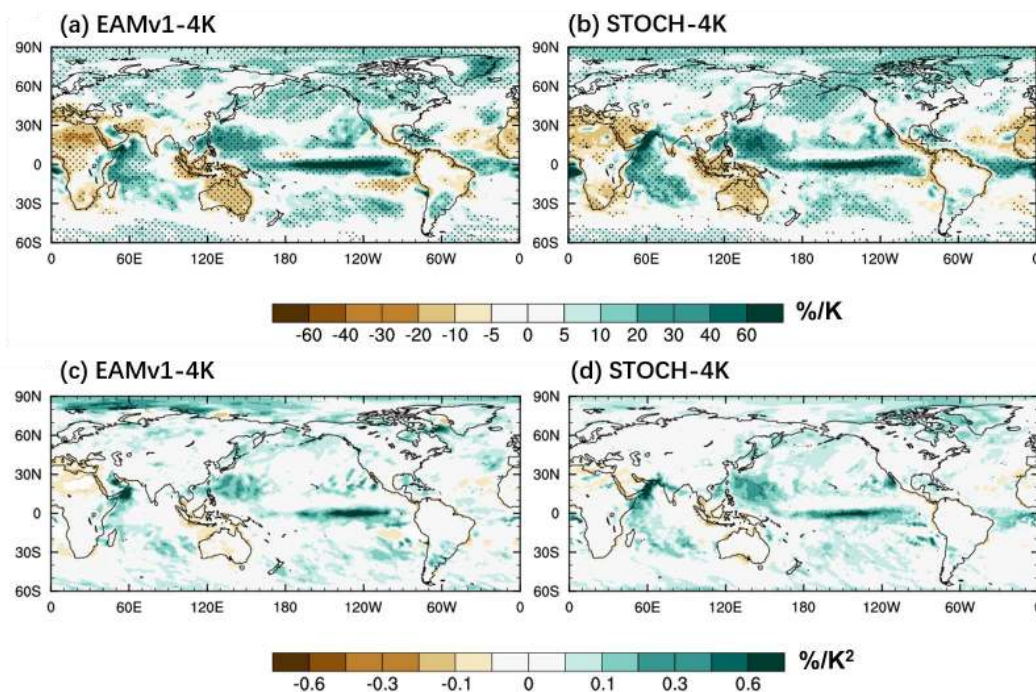
845



846

847 **Figure 13.** Taylor diagram with metrics for STOCH, compared with EAMv1.

848



849

850 **Figure 14.** Geographical distributions of responses of (a&b) annual mean precipitation and (c&d)  
851 precipitation extremes (R95p) to climate warming from +4K experiments. Differences with a  
852 confidence level greater than 95% are stippled.